

HOTS3D: Hyper-Spherical Optimal Transport for Semantic Alignment of Text-to-3D Generation

Zezeng Li, Weimin Wang, Wenhai Li, Na Lei, and Xianfeng Gu

Abstract—Recent CLIP-guided 3D generation methods have achieved promising results but struggle with generating faithful 3D shapes that conform with input text due to the gap between text and image embeddings. To this end, this paper proposes HOTS3D which makes the first attempt to effectively bridge this gap by aligning text features to the image features with spherical optimal transport (SOT). However, in high-dimensional situations, solving the SOT remains a challenge. To obtain the SOT map for high-dimensional features obtained from CLIP encoding of two modalities, we mathematically formulate and derive the solution based on Villani’s theorem, which can directly align two hyper-sphere distributions without manifold exponential maps. Furthermore, we implement it by leveraging input convex neural networks (ICNNs) for the optimal Kantorovich potential. With the optimally mapped features, a diffusion-based generator and a Nerf-based decoder are subsequently utilized to transform them into 3D shapes. Extensive qualitative and quantitative comparisons with state-of-the-arts demonstrate the superiority of the proposed HOTS3D for 3D shape generation, especially on the consistency with text semantics. The code will be publicly available.

Index Terms—Text-to-3D generation, spherical optimal transport, semantic alignment, 3D generation, mesh

1 INTRODUCTION

TEXT-TO-3D generation endeavors to create 3D assets that are coherent with the input texts, which has the potential to benefit a wide array of applications such as animations, games, architecture, and virtual reality. Despite the extensive needs, the production of premium 3D content often remains a daunting task. The traditional process of creating 3D assets requires a significant investment of time and effort, even when undertaken by professional designers [1]. This challenge has prompted the development of text-to-3D methods. Recently, with the development of large language models (LLM) and large-scale datasets, deep learning based text-to-3D models [2]–[13] have made remarkable progress and can generate diverse shapes from various text prompts. The existing text-to-3D methods are either CLIP-guided end-to-end methods or optimization-based methods. The former trains a mapper from the CLIP [14] image embeddings to the shape embeddings of a 3D shape generator and switches to the CLIP text embedding as the input at test phase [2], [8], [15]–[18]. The latter iteratively optimizes the CLIP similarity loss between a text prompt and renders images of a 3D scene representation [3]–[5], [19], [20] or the score distillation sampling loss [6], [7], [9], [10] to achieve semantic alignment.

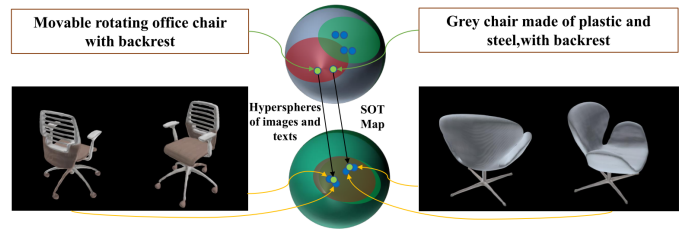


Fig. 1: Semantic alignment with the proposed SOT map. Texts and images are embedded onto hyper-spheres by CLIP encoders. However, feature distributions (ellipse regions) of two modalities may not be well aligned. SOT learns to optimally transport features to align them and thus enhances the semantic consistency of generated shapes.

CLIP-guided optimization-based methods typically exhibit superior text-shape consistency. However, they require re-optimizing model parameters for each text input, resulting in significant generation time costs. For instance, DreamFields [5] takes over 30 minutes to generate a single 3D shape from a given text. In contrast, the CLIP-guided end-to-end methods demonstrate notably faster generation speed with acceptable quality. Despite their efficiency, these methods often overlook the gaps between text and image features as illustrated in the upper sphere in Fig. 1. This usually leads to the mismatching problem and semantic inconsistency of generated 3D shapes, especially in the testing stage which treats the two equally. Besides, as remarked in Dream3D [20], CLIP-guided methods tend to generate unconstrained “adversarial contents” that achieve high CLIP scores but with poor text consistency. To narrow the domain gap, Dream3D iteratively optimizes a text-to-image diffusion model, achieving more coherent results than other baselines. Nevertheless, as a CLIP-guided optimization-based method, Dream3D inherently suffers from extended sam-

- This research was supported by the National Key R&D Program of China under Grant No. 2021YFA1003003; the Natural Science Foundation of China under Grant No. 61936002, No. T2225012 and No. 62306059.
- W. Wang and N. Lei are with the International Information and Software Institute, Dalian University of Technology, Dalian, 116620, China (Email: wangweimin@dlut.edu.cn, nalei@dlut.edu.cn).
- Z. Li and W. Li are with the School of Software, Dalian University of Technology, Dalian, 116620, China (Email: zezeng.lee@gmail.com, wenhai@mail.dlut.edu.cn).
- X. Gu is with the Department of Computer Science and Applied Mathematics, State University of New York at Stony Brook, Stony Brook, NY 11794-2424, USA (Email: gu@cs.stonybrook.edu).
- Equal contribution: Zezeng Li, Weimin Wang.
- Corresponding author: Na Lei (Email: nalei@dlut.edu.cn).

pling duration, which is further exacerbated by an additional diffusion process.

To improve the semantic consistency of text-to-3D generation while maintaining efficiency, we consider introducing optimal transport (OT) to align semantics and image features. Increasing OT-based methods are successfully applied in image generative models to align prior distribution for high quality and diverse generation [21]–[25]. However, they typically operate in Euclidean space, while there exists the constraint of normalization on the hyper-sphere for CLIP-guided text and image features, i.e. spherical optimal transport (SOT). Furthermore, solutions of SOT are relatively less investigated. Especially for hyper-spheres, the implementation is significantly challenging due to the high dimension.

To this end, we formulate and derive the SOT map for high-dimensional semantic and image feature distribution alignment, leading to a novel hyper-sphere-OT-based end-to-end text-to-3D generative model, named **HOTS3D**. For the implementation of SOT, we approach SOT as a spherical Kantorovich dual problem and employ two input convex neural networks (ICNN) [26] to represent two convex potentials [27], whose gradients are pivotal in solving the SOT map. Once the solution is extrapolated through the learning process, optimally mapped features are decoded into 3D shapes. Our main contributions are:

- We are the first to formulate semantic alignment as a hyper-sphere OT problem for end-to-end text-to-3D generation. With the observation of hyper-spherical distributions of CLIP features, we propose to optimally transport text features to image features on hyper-spheres to bridge the semantic gap.
- We mathematically derive the solution of SOT on hyper-spheres for CLIP-extracted features. Furthermore, we design a whole pipeline for SOT learning and semantic alignment in text-to-3D generation.
- We perform extensive experiments and analysis, which verify the superiority of the proposed **HOTS3D** in terms of semantic consistency and quality (lower FID score) compared with state-of-the-art methods.

2 RELATED WORK

2.1 Text-to-3D content generation

With the development of CLIP [14] technology and the need for 3D content creation, text-to-3D generation has attracted considerable attention [5]–[7], [11], [28]–[31]. Existing methods can be categorized CLIP-guided **end-to-end generative models** with pretrained [2], [8], [15]–[18], [32]–[37] or finetuned CLIP encoders [38]–[40], and CLIP-guided **optimization based methods** [3]–[7], [9], [10], [19], [20], [41]–[43]. End-to-end generative models attempt to learn the distribution of the entire dataset, so that they can process different text inputs and generate various 3D assets without any fine-tuning. Optimization-based methods achieve bimodal alignment by iteratively optimizing the similarity between input text and the rendered images of the generated 3D assets. For those methods, it is necessary to finetune the model for each text, and the generation process is time-consuming.

In this work, we focus on end-to-end generative models. Among those existing methods, Shap-E [18] is most relevant

to this paper, which can generate diverse objects without relying on images as an intermediate representation and has gained popularity in the research community due to its impressive results. Recently, Diffusion-SDF [17] proposed an SDF autoencoder together with the voxelized Diffusion model to learn and generate representations for voxelized signed distance fields (SDFs) of 3D shapes. SDFusion [8] enables 3D shape completion, reconstruction, and generation using a diffusion-based encoder-decoder. These CLIP-guided text-to-3D content generation methods have yielded impressive results, but as remarked in Dream3d [20], they overlooked the gap between the text and image embedding spaces. Consequently, semantic alignment is the key to filling this gap and improving text-shape consistency.

2.2 Semantic alignment

Most text-to-3D generation methods are proposed based on the assumption that image features and text features correspond in the cross-modal embedding space, which is usually extracted by CLIP. Due to the issue of inconsistent text shapes in generation models, more and more researchers are attempting to align semantic and image features further to improve text-shape consistency. For example, Li et al. [44] introduced a contrastive loss to align the image and text representations, making it easier for the multimodal encoder to perform cross-modal learning. Cheng et al. [45] designed a semantic alignment module to fully explore the latent correspondence between images and text. Guo et al. [46] modeled the distribution over discrete motion tokens which enables non-deterministic production of variable lengths pose sequences for input texts. 3D-VisTA [47] utilized a pre-trained Transformer for point cloud and text alignment which eliminates the need for auxiliary losses and optimization tricks in question answering tasks. Nie [48] mined the semantic consistency by compacting each 3D shape and its nearest neighbors to enhance semantic alignment for unlabeled 3D model domains. Cao [49] developed a cross-modal alignment module to align feature spaces between 3D point cloud and image/text modalities. For consistent generation, Zhao [50] proposed to use one network to encode the 3D shapes into the shape latent space aligned to the image and text, and use another network to learn a probabilistic map from the image or text space to the latent shape space. Liu et al. [38], [41], [42] finetuned the text encoder to improve the text-shape consistency. Xu et al. [20] bridged the text and image modalities with a diffusion model. These methods either only fine-tune the model from the perspective of cosine similarity, or require complex and time-consuming diffusion models, which motivates us to explore more effective semantic alignment methods.

2.3 Euclidean and spherical optimal transport

The OT map transmits one distribution to another in the most cost-effective manner, which has been widely applied for **distribution alignment** in Euclidean space [21]–[25], [51]–[57]. Recently, several works have shown that using a prior on the hyper-sphere can improve the results [58]–[61]. Contrary to Euclidean geometry, both the metric and the transportation costs under the spheres differ, leading to the traditional OT algorithms being ineffectual for spheres. Consequently, OT solutions for spheres or hyper-spheres have

attracted community attention. Cui et al. [62] provided a **2D SOT** algorithm from a geometric view to adjust the density of triangular facets for mesh parameterization. Later, Hamfeldt et al. [63], [64] proposed a PDE approach to numerically solving the 2D SOT map and constrains the solution gradient to obtain a stable scheme. Cohen et al. [65] designed a flow model based on the Riemannian exponential map to fit the 2D SOT. However, due to the challenge of calculating Jacobian determinants (JD) in high-dimension, stochastic trace estimates need to be used to approximate JD for distribution transformation. Bonet et al. [65] defined spherical sliced-Wasserstein (SSW) distances on Riemannian manifolds and utilized the Flow model [65] to fit the 2D SOT by minimizing the SSW loss. In high-dimensional cases, SSW was taken as a regularization term to guide the decoder to output a feature distribution aligning with the prior distribution, but the map fitted by the decoder is not an SOT map. For the **hyper-sphere OT**, Rezende et al. [66] designed a Hessian matrix to reformulate the Kantorovich potential and gave a threshold criterion of the matrix for the hyper-sphere. Nonetheless, due to the difficulty in calculating the JD, only 2D SOT validation experiments were provided. As remarked in [66], solving the SOT problem in high-dimensional settings based on exact likelihoods is still challenging. Moreover, SOT algorithms like Ref [65], [66] used Riemannian exponential maps to switch Euclidean data to hyper-spheres and then calculated the OT map in a Euclidean way, which inevitably leads to distortion of manifolds and accuracy decline of results.

3 METHOD

Our objective is to generate 3D content that aligns with the given input text prompt. As illustrated in Fig. 2, our framework for text-guided 3D synthesis comprises four stages. Firstly, we encode the input text prompt onto the hyper-sphere with a pre-trained CLIP text encoder, obtaining text features. Secondly, the SOT map in Eq.(15) is induced by the gradient of a convex function (see Fig. 3) that is trained via minimax optimization, and then transfers output text features to the image feature space. In the third stage, a generator conditioned on the output of the SOT Map was utilized to generate 3D shape priors. This process involves a diffusion process based on a cross-attention score network. Finally, a Nerf-based decoder was utilized to decode the generated shape priors into 3D shapes. The SOT map is a plug-and-play tool for aligning spherical distributions. During the training phase, we only need to optimize the parameters of the SOT map and other modules remain frozen, significantly reducing the training difficulty.

Observations and Motivations. Though CLIP-guided end-to-end generative methods can generate diverse results, they are short in producing precise and detailed 3D structures that accurately match the text, as depicted in Fig. 5. Its cause lies in the gaps between text and image features, especially in the testing stage, treating the two equally, directly leading to a mismatch issue. To narrow this gap, CLIP-guided optimization methods attempt to align the semantics of instance text through iteration, resulting in significant time costs. Thus, from the perspective of **distribution alignment**, we propose using SOT Map to transfer entire text features into

the image space. For solutions of SOT, existing works are either not applicable to hyper-sphere, or cause distortion, which encourages us to design a more effective method.

Compared with existing distribution alignment methods (e.g., GAN and VAE-based), the method proposed in this paper has the following advantages and theoretically essential differences: 1) Space: our alignment is in hypersphere space, while most others are in Euclidean space. 2) Align approach: ours fits a convex potential function whose gradient induces the transport map, while others fit the map with neural nets. Thus, they cannot represent discontinuous target distributions, leading to mode mixture (mixed generation) results across boundaries. Conversely, ours can align distributions with discontinuous support while maintaining clear boundaries, as shown in Fig. 6.

3.1 Problem formulation and preliminary

Given text feature set $\mathbf{X} \subset \mathbb{S}^d$, image feature $\mathbf{Y} \subset \mathbb{S}^d$, and their respective prescribed probability measure μ_S and ν_S , our goal is to transfer text features to the image feature space to achieve alignment of two modalities, thereby providing more accurate features encoding for generations. In the following, we introduce relevant OT theories to provide preliminary for subsequent method explanations.

Optimal Transport (OT). Let μ and ν be two probability distributions on \mathbb{R}^d . The *Monge’s optimal transport problem* is to transport the probability mass under μ to ν with the minimum total transportation cost, *i.e.*

$$\min_{T: T_{\#}\mu=\nu} \mathbb{E}_{\mathbf{X}\sim\mu} c(\mathbf{X}, T(\mathbf{X})). \quad (1)$$

Where T achieving the minimum total cost in Eq. (1) is called OT map. $T_{\#}\mu$ is the push-forward of μ under T . Subsequently, by combining the joint distribution, Kantorovich relaxed the original *Monge’s OT problem* and provided a dual formulation *Kantorovich duality problem* [27],

$$W_d(\mu, \nu) = \sup_{(f, g) \in \Phi_c} \mathbb{E}_{\mu}[f(\mathbf{X})] + \mathbb{E}_{\nu}[g(\mathbf{Y})], \quad (2)$$

where Φ_c denotes the constrained space of Kantorovich potentials, defined as $\Phi_c \triangleq \{(f, g) \in L^1(\mu) \times L^1(\nu) : f(\mathbf{x}) + g(\mathbf{y}) \leq c(\mathbf{x}, \mathbf{y}), \forall (\mathbf{x}, \mathbf{y}) \text{ d}\mu \otimes \text{d}\nu \text{ a.e.}\}$. $c(\mathbf{x}, \mathbf{y})$ is the cost function. The optimal transport map can be obtained from f and g , using the first-order optimality conditions of the Fenchel-Rockafellar’s duality theorem [21], or by training a generator through an adversarial optimization [52]. f and g play a symmetric role in Eq. (2), and either of them can be replaced by the other’s c -transform. The c -transform of g is defined by $g^c(\mathbf{x}) = \inf_{\mathbf{y}} (c(\mathbf{x}, \mathbf{y}) - g(\mathbf{y}))$. Then, as it is remarked in [67, Theorem 5.26] and [68], [69, Definition 3.3 & 3.6], the Kantorovich problem can be reformulated as the following dual problem:

$$W_d(\mu, \nu) = \sup_{g \in L^1(\nu)} \mathbb{E}_{\mu}[g^c(\mathbf{X})] + \mathbb{E}_{\nu}[g(\mathbf{Y})], \quad (3)$$

Spherical Optimal Transport (SOT). Given two prescribed probability measure μ_S and ν_S on \mathbb{S}^d , we seek a spherical map $T : \mathbb{S}^d \rightarrow \mathbb{S}^d$ such that

$$T = \min_{T_{\#}\mu_S=\nu_S} \mathbb{E}_{\mathbf{X}\sim\mu_S} c(\mathbf{X}, T(\mathbf{X})). \quad (4)$$

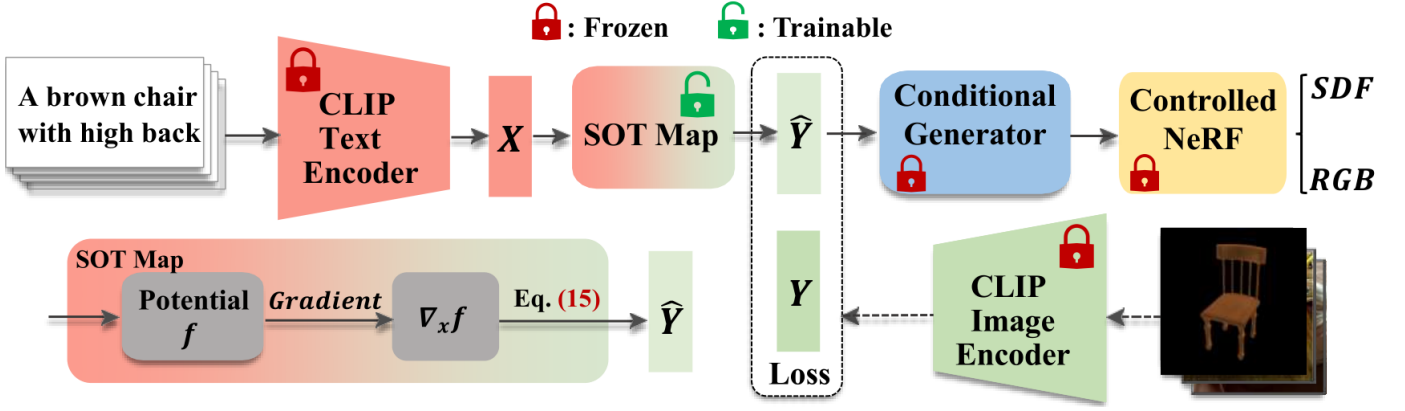


Fig. 2: Overview of the proposed text-to-3D framework with the SOT map defined in Eq. (15). The dotted line indicates the process only in the Potential function training phase to solve the SOT map. The Loss is calculated by Eq. (16) and Eq. (17).

Here $c(\mathbf{x}, \mathbf{y})$ is the cost of transporting a unit of mass from \mathbf{x} to \mathbf{y} . $\langle \cdot, \cdot \rangle$ denotes the vector inner product. $T_{\#}\mu_S = \nu_S$ indicates $\int_{\mathbf{X}} \mu_S(\mathbf{x}) d\mathbf{x} = \int_{T(\mathbf{X})} \nu_S(\mathbf{y}) d\mathbf{y}$ for every measurable $\mathbf{X} \subset \mathbb{S}^d$, $\mathbf{Y} \subset \mathbb{S}^d$. Similarly, the spherical Kantorovich dual problem has the same form as Eq. (2).

3.2 Derivation of SOT solution on hyper-sphere

Given the logarithmic transportation cost $c(\mathbf{x}, \mathbf{y}) = \log(2 - \langle \mathbf{x}, \mathbf{y} \rangle)$ which is the widely used on spheres, potential pair $(f, g) \in \Phi_c$ satisfy

$$f(\mathbf{x}) + g(\mathbf{y}) \leq \log(2 - \langle \mathbf{x}, \mathbf{y} \rangle). \quad (5)$$

To directly calculate the OT map on hyper-spheres, we reformulate dual problem in Eq. (3) into the following form involving only a single convex function g :

$$W_d = \sup_{g \in \text{CVX}(\nu_S)} \mathbb{E}_{\mu_S}[g^c(\mathbf{X})] + \mathbb{E}_{\nu_S}[g(\mathbf{Y})]. \quad (6)$$

Here $\text{CVX}(\nu)$ denotes the set of all convex functions in $L^1(\nu)$, $g^c(\mathbf{x}) = \inf_{\mathbf{y}} (\log(2 - \langle \mathbf{x}, \mathbf{y} \rangle) - g(\mathbf{y}))$ is the conjugate c-transform of $g(\cdot)$.

According to [67, Theorem 5.26], any optimal pair potential (g, g^c) in Eq. (6) induce an OT map pushing forward ν_S onto μ_S , and (f, f^c) induce an OT map pushing forward μ_S onto ν_S . Specifically, if $c(\mathbf{x}, \mathbf{y}) = \frac{1}{2}\|\mathbf{x} - \mathbf{y}\|^2$, the OT map $T(\mathbf{x}) = \mathbf{x} - \nabla f(\mathbf{x})$. When we shift our attention to hyper-spheres, this solution no longer applies. To provide a functional relationship between the OT map and Kantorovich's potential on hyper-spheres, we introduce some theorems below.

Theorem 3.1. ([67, Villani]). Given μ and ν on a compact convex domain $\Omega \subset \mathbb{R}^d$, there exists an OT plan for the cost $c(\mathbf{x}, \mathbf{y}) = h(\mathbf{x} - \mathbf{y})$, with h strictly convex. It is unique and of the form $(\text{id}, T_{\#})\mu$ (id: identity map), provided that μ is absolutely continuous and $\partial\Omega$ is negligible. Moreover, there exists a Kantorovich's potential φ , and the OT map T can be represented as follows:

$$T(\mathbf{x}) = \mathbf{x} - (\nabla h)^{-1}[\nabla\varphi(\mathbf{x})] \quad (7)$$

This theorem was first explained by Villani [67] and later organized by Lei et al. [68], [69]. Based on it, we further provide an explicit functional relationship between the OT

map and Kantorovich's potential φ , in the case of hyper-spheres.

Theorem 3.2. Suppose $\mathbf{X} \subset \mathbb{S}^d$, $\mathbf{Y} \subset \mathbb{S}^d$ are two subsets of d -dimensional hyper-sphere \mathbb{S}^d , and μ_S and ν_S are two probability measures defined on \mathbf{X} and \mathbf{Y} , respectively. Given cost $c(\mathbf{x}, \mathbf{y}) = \log(2 - \langle \mathbf{x}, \mathbf{y} \rangle)$, there exists a Kantorovich's potential φ such that the OT map $T : \mathbf{X} \rightarrow \mathbf{Y}$ can be represented as follows:

$$T(\mathbf{x}) = \mathbf{x} - \frac{\nabla\varphi(\mathbf{x})}{1 - \mathbf{x}^T \nabla\varphi(\mathbf{x})} \quad (8)$$

Proof. Assume $\mathbf{z} = \mathbf{x} - \mathbf{y}$, then, based on Theorem 3.1, we get $h(\mathbf{z}) = \log(2 - \langle \mathbf{x}, \mathbf{y} \rangle)$. The gradient and Hessian matrix of h regarding \mathbf{z} are as follows:

$$\nabla h(\mathbf{z}) = \frac{\mathbf{x} - \mathbf{y}}{2 - \mathbf{x}^T \mathbf{y}} \quad (9)$$

$$h''(\mathbf{z}) = \frac{2(2 - \mathbf{x}^T \mathbf{y})\mathbf{1}\mathbf{1}^T + \mathbf{z}\mathbf{z}^T}{(2 - \mathbf{x}^T \mathbf{y})^2} \quad (10)$$

The Hessian matrix in Eq. (10) is positively definite, therefore h is strictly convex. Suppose $(\mathbf{x}_0, \mathbf{y}_0)$ is a point in the support of T , by definition $\varphi^c(\mathbf{y}_0) = \inf_{\mathbf{x}} (c(\mathbf{x}, \mathbf{y}_0) - \varphi(\mathbf{x}))$, hence, $\nabla_{\mathbf{x}}(c(\mathbf{x}, \mathbf{y}_0) - \varphi(\mathbf{x}))|_{\mathbf{x}=\mathbf{x}_0} = 0$. Then, we get

$$\nabla\varphi(\mathbf{x}_0) = \nabla_{\mathbf{x}}c(\mathbf{x}_0, \mathbf{y}_0) = \nabla h(\mathbf{x}_0 - \mathbf{y}_0) \quad (11)$$

Combining Eq. (10), we obtain

$$\nabla\varphi(\mathbf{x}) = \frac{\mathbf{x} - \mathbf{y}}{2 - \mathbf{x}^T \mathbf{y}} \quad (12)$$

$$\mathbf{z} = [2 - \mathbf{x}^T(\mathbf{x} - \mathbf{z})]\nabla\varphi(\mathbf{x}) = (1 + \mathbf{x}^T \mathbf{z})\nabla\varphi(\mathbf{x}) \quad (13)$$

Suppose $\mathbf{z} = \lambda\nabla\varphi(\mathbf{x})$, then we get

$$\begin{aligned} \lambda\nabla\varphi(\mathbf{x}) &= (1 + \lambda\mathbf{x}^T \nabla\varphi(\mathbf{x}))\nabla\varphi(\mathbf{x}) \\ &\Rightarrow \lambda(1 - \mathbf{x}^T \nabla\varphi(\mathbf{x})) = 1 \\ &\Rightarrow \lambda = \frac{1}{1 - \mathbf{x}^T \nabla\varphi(\mathbf{x})} \Rightarrow \mathbf{z} = \frac{\nabla\varphi(\mathbf{x})}{1 - \mathbf{x}^T \nabla\varphi(\mathbf{x})} \\ &\Rightarrow \mathbf{y} = \mathbf{x} - \mathbf{z} = \mathbf{x} - \frac{\nabla\varphi(\mathbf{x})}{1 - \mathbf{x}^T \nabla\varphi(\mathbf{x})} \end{aligned}$$

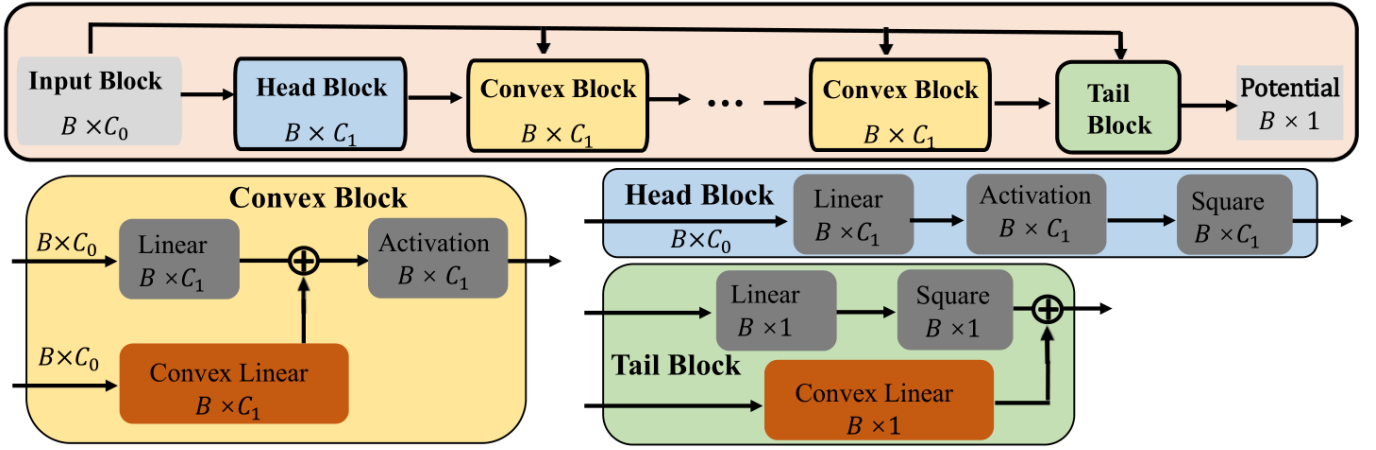


Fig. 3: Network architecture of potential functions f and g . B denotes the batch size. C_0 and C_1 are the dimensions of the input features and hidden layer features, respectively. \oplus is the addition in mathematics.

Theorem 3.2 provides the explicit functional relationship between the SOT map and potential φ . However, the objective Eq. (6) is not amenable to standard stochastic optimization schemes due to the conjugate function g^c . To this end, we propose a novel minimax formulation in the following proposition, where we replace the \mathbf{y} in g^c with the transport map $T_f(\mathbf{x})$ defined in Eq. (15) on \mathbf{X} .

Proposition 3.3. Given two probability measures μ_S and ν_S which are defined on $\mathbf{X} \subset \mathbb{S}^d$ and $\mathbf{Y} \subset \mathbb{S}^d$, respectively. We have

$$W_d = \sup_{g \in \text{CVX}(\nu_S)} \inf_{f \in \text{CVX}(\mu_S)} \mathbb{E}_{\nu_S} g(\mathbf{Y}) + \mathcal{V}_{\mu_S}(f, g) \quad (14)$$

where $\mathcal{V}_{\mu_S}(f, g)$ is a functional of f, g defined as

$$\mathcal{V}_{\mu_S}(f, g) = \mathbb{E}_{\mu_S} [\log(2 - \langle \mathbf{X}, T_f(\mathbf{X}) \rangle) - g(T_f(\mathbf{X}))]$$

where $T_f(\mathbf{X})$ is a functional of f defined as

$$T_f(\mathbf{x}) = \mathbf{x} - \frac{\nabla f(\mathbf{x})}{1 - \mathbf{x}^T \nabla f(\mathbf{x})}. \quad (15)$$

Proposition 3.3 transforms the solution of the SOT map into the problem of optimizing the W_d with f and g as variables. Its advantage lies in establishing a direct connection between the f and g and transforming the infimum calculation of c-transform into a parameter optimization process during the learning. Moreover, the gradient of potential f induces the SOT map which can fit discontinuous maps and allows to keep sharp boundaries.

According to Theorem 3.2, there exists a potential function f such that $T_f : \mathbf{X} \rightarrow \mathbf{Y}$ in Eq. (15) satisfies (4). This indicates that there exists an optimal pair (f_0, g_0) achieving the infimum and supremum respectively, and T_{f_0} is the OT map from μ_S to ν_S . In other words, T_{f_0} maps \mathbf{X} to \mathbf{Y} in a measure preserving manner, satisfying $T(\mathbf{X}) = \mathbf{Y}$. Thus, the solution for Eq. (6) is also a solution for Eq. (14). Based on this, the next pertinent question is how to construct a suitable f and g , and how to effectively solve this optimization problem.

Algorithm implementation for SOT learning. Inspired by Makkuva et al. [70], we instantiated the Kantorovich

potential f and g with ICNN [26], where ICNNs are a specific parametric class of convex functions with rich enough representation. The network architecture of potential f and g is shown in Fig. 3. Specifically, in our experiment, we set $C_0 = 768$ and $C_1 = 1024$, respectively. Further, to improve the text-shape consistency, we add a fidelity loss to the objective (16), where the $d(T_f(\mathbf{x}), \mathbf{y}) = \cos^{-1}(\langle T_f(\mathbf{x}), \mathbf{y} \rangle)$ is the spherical distance between the output and the paired image feature. λ is the weight, which was set to 1 in our experiment. Finally, the desired f and g pair is obtained by a training procedure with alternate optimization: *i) Potential f is optimized by Eq. (16); ii) Potential g is optimized by Eq. (17).*

$$\inf_{f \in \text{CVX}(\mu_S)} [\mathcal{V}_{\mu_S}(f, g) + \lambda \mathbb{E}_{\mu_S} d(T_f(\mathbf{X}), \mathbf{Y})], \quad (16)$$

$$\sup_{g \in \text{CVX}(\nu_S)} [\mathbb{E}_{\nu_S} g(\mathbf{Y}) - \mathbb{E}_{\mu_S} g(T_f(\mathbf{X}))]. \quad (17)$$

3.3 Text-to-3D generation with SOT map

After we get the well-optimized potential f , the SOT map $T_f(\mathbf{x})$ from text feature hyper-sphere $\mathbf{X} \subset \mathbb{S}^{767}$ to image feature hyper-sphere $\mathbf{Y} \subset \mathbb{S}^{767}$, can be obtained with Eq. (15) to achieve semantic alignment. For input texts, we utilize CLIP to obtain the initial embedded text features. In previous approaches, text features were directly used as image features for generation. To bridge the gap between the image and text features, we apply the obtained powerful SOT map to project text feature \mathbf{X} to the aligned $\hat{\mathbf{Y}}$ in the CLIP embedding space. Apart from cosine similarity, the SOT map also aligns the two modalities from the view of global distribution. Thereafter, as illustrated in Fig. 2, a diffusion-based conditional generator and a controlled NeRF model are followed to transform the output feature to signed distance functions (SDFs) and texture color. To construct a triangle mesh, a differentiable Marching Cubes [71] is adopted.

We train the SOT map by extracting the text embeddings and corresponding image embeddings from shape renderings using the CLIP ViT-L/14 [14] encoder. The conditional generator and a controlled NeRF are based on an open-source Shap-E implementation [18]. More specifically, the

conditional generator is implemented by a conditional diffusion model of $MLP+Transformer+MLP$, where the first MLP is for combining the conditional CLIP embedding, and the latter MLP is for the implicit field. A NeRF-based decoder is followed to render the obtained implicit field and extract the SDF for mesh generation.

4 EXPERIMENTS

Section 3 analyzes the benefits of our proposed text-to-3D generation framework **HOTS3D** from the theoretical perspective, and then we will further evaluate the performance of HOTS3D experimentally. The experimental results indicate that HOTS3D has the following pros: **1)** it serves as a plug-and-play tool for semantic alignment of CLIP-guided models; **2)** the text-3D consistency of shape generated by our model has been drastically enhanced.

4.1 Setup

4.1.1 Datasets

The text prompts are from dataset Text2Shape [15] which provides descriptions for the ‘chair’ and ‘table’ categories in ShapeNet. These text prompts we utilized for testing are the first 1800 text prompts of Text2Shape test dataset. Specifically, we synthesize 2 shapes for each prompt from 1800 text prompts, then, employ Blender [72] to render 20 images for each synthesized 3D mesh, which were used for metrics calculation in subsequent experiments. The ground truth images are obtained by choosing the corresponding mesh from ShapeNet and rendering 20 views for each shape. All image sizes are uniformly set to 512×512 . When rendering the view, we set up simple lighting and materials: all models were rendered using a fixed lighting configuration that only supports diffuse and ambient shading. In Fig. 4, several exemplary text-image pairs are shown. For simplicity, each shape only displays an image from one view.

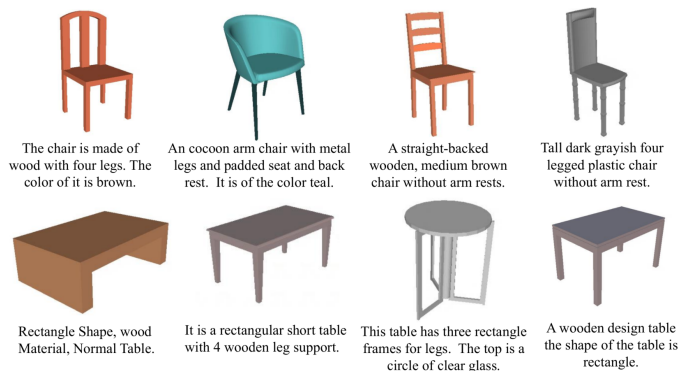


Fig. 4: Example text-image pairs of Text2Shape dataset.

4.1.2 Baseline Methods

We compare our method with six state-of-the-art methods, including four end-to-end generative models: CLIP-Forge [2], Shap-E [18], SDFusion [8], TAPS3D [33], as well as two optimization based methods: PureCLIPNeRF [3] and CLIP-Mesh [19]. For a fair comparison, we conduct tests using the default settings, official implementations, and pre-training models for all baseline methods.

Method	CLIP R-Precision \uparrow		FID \downarrow	LFD \downarrow	S-A100
	ViT-B/32	ViT-L/14			
CLIP-Forge [2]	55.7	56.5	158.6	8621	260.9
Shap-E [18]	69.8	68.3	92.1	6945	7.1
SDFusion [8]	72.3	72.8	173.8	5929	8.9
TAPS3D [33]	66.6	67.6	139.2	7530	9.7
Ours	79.3	80.1	42.6	5349	10.2
PureCLIPNeRF [3]	82.8	81.0	172.3	-	1597.9
CLIP-Mesh [19]	-	-	-	-	7366.9

TABLE 1: Quantitative comparison on Text-to-3D generation. Two distinct models are utilized to compute the CLIP R-Precision. S-A100 denotes the average time (in seconds) it takes to generate 20 images of a shape for a text on the NVIDIA Tesla A100 GPU. Methods of the last two rows are CLIP-guided optimization-based.

Specifically, CLIP-Forge is a zero-shot text-to-shape generative model that addresses the scarcity of paired data. Shap-E, a latent diffusion model over a space of 3D implicit functions, can render both NeRFs and textured meshes. Due to its extensive training dataset and diverse generation capabilities, Shap-E serves as the backbone model for our HOTS3D. SDFusion employs diffusion models for signed distance functions, facilitating various applications such as 3D shape generation, shape completion, and texture generation. TAPS3D focuses on textured shape generation and is trained with the ShapeNet Table and Chair classes. PureCLIPNeRF optimizes model parameters by predicting the density and color corresponding to voxels, with text-based generation relying solely on CLIP [14]. Finally, CLIP-Mesh generates textured meshes through continuous optimization of the vertex coordinates and corresponding texture maps of the initial mesh.

4.1.3 Evaluation Metrics

For the qualitative evaluation, we employ FID [73] and LFD [74] score to assess the quality of the generated shapes. FID measures the distance between the distribution of the rendered images and the ground truth image distribution. LFD measures the dissimilarity between a groundtruth mesh and a generated mesh with rendered images from 60 views. Both FID and LFD indicate higher quality with lower scores. Moreover, to measure the consistency between the generated shapes and input text, we report the CLIP retrieval precision (CLIP R-Precision) [75] on the test dataset with diverse text prompts and objects. This metric quantifies the percentage of generated images that the CLIP encoder associates with the correct text prompt used for generation. For a fair comparison, we followed CLIP R-Precision [75] to calculate the top-10 retrieval accuracy when retrieving the matching text from 100 candidates using the generated image as a query.

4.2 Experiment Results

4.2.1 Implementation Details

We only need to train SOT for the whole network, while other modules remain frozen. Specifically, we utilize the CLIP ViT-L/14 encoder to extract text features as input and image features of rendered shapes as ground truth for SOT

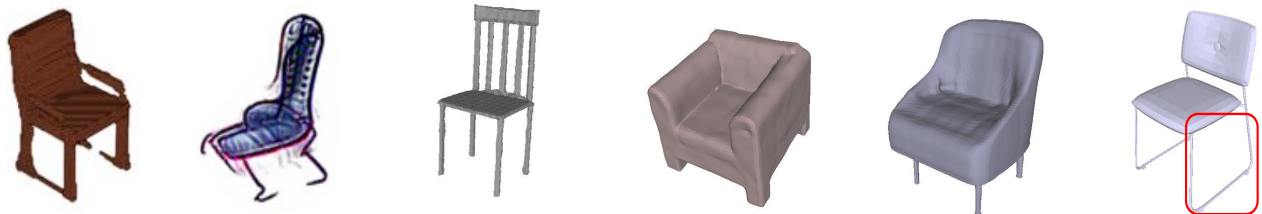
A wooden coffee table with legs inside to look like **2 tables hooked together**.



Around wooden table with one leg in the center and **a small square base**.



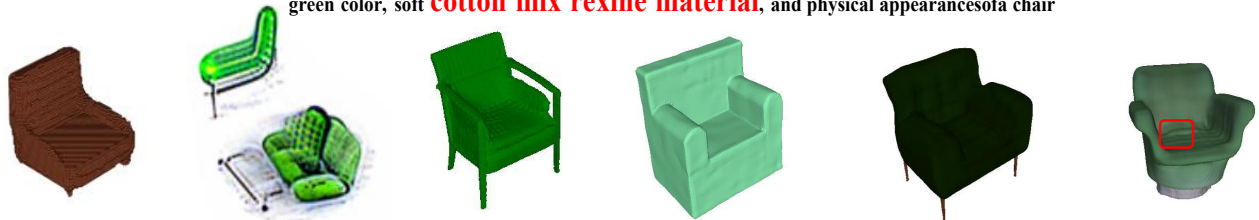
A chair with cushions and **U shaped legs**.



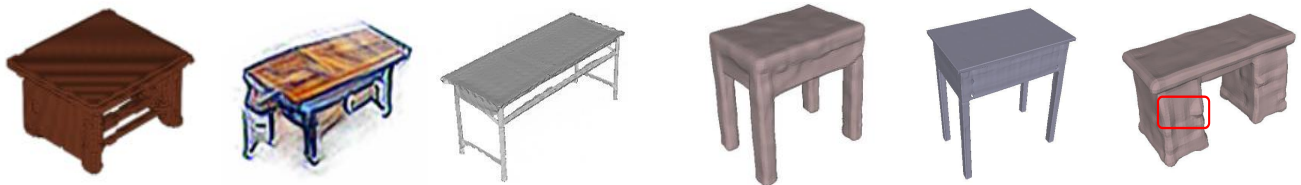
Adirondack chair, made of brown wood slats that sits low to the ground.



green color, soft **cotton mix rexine material**, and physical appearance of a chair



A solid looking simple table **with a drawer**.



CLIP-Forge

PureCLIPNeRF

TAPS3D

SDFusion

Shap-E

Ours

Fig. 5: Qualitative comparison. The corresponding text is displayed above each row and the text in the red box is the corresponding area for distinctive description.

training with objectives defined in Eq. (15) and Eq. (16) of our main manuscript. The weight λ in Eq. (15) was empirically set to 1 in our experiment. The learning rate is 10^{-4} , and the optimizer is Adam [76]. Training the SOT map on the dataset Text2Shape [15] takes approximately 28 hours

with a Tesla A100 GPU.

4.2.2 Quantitative Results

We report the CLIP retrieval precision metrics and FID in Tab. 1, and both the CLIP ViT-B/16 and CLIP ViT-B/32 encoders are employed as retrieval models. Compared to the

first four CLIP-guided end-to-end generative models, our HOTS3D achieves the highest CLIP R-Precision with both retrieval models. Compared to optimization-based methods, our HOTS3D can achieve comparable performance with significantly lower time costs. By leveraging the SOT map, our method bridges the modality gap between text and image features and thus can generate more faithful 3D structures to the input text. Moreover, with the SOT map, we can compensate for the missing detailed information in texts composed of high-level semantics. Consequently, our method exhibits a significantly lower FID score compared to these baseline methods.

To investigate whether semantic alignment can benefit shape quality, we evaluated the dissimilarity between real meshes and generated meshes using the LFD metric, as shown in Tab. 1. Since PureCLIPNeRF [3] outputs rendered images from different views instead of meshes, it cannot be evaluated using LFD. Additionally, CLIP-Mesh [19] was excluded from the comparison due to its lengthy generation time. As seen in Tab. [19], our method achieved the best LFD score, indicating that it produces high-quality 3D shapes consistent with the target objects.

We also present a comparison of the generation efficiency of a single text. As shown in the Tab. 1, CLIP-guided optimization methods [3], [19] require training the model for each input text, so it often takes tens of minutes to process a single text input well. Especially for CLIP-Mesh, it takes over two hours to process a text. Due to issues of expensive time costs, we abandoned the metric score test for CLIP-Mesh. In comparison, our method can generate a 3D shape that is high-quality and highly consistent with the input text in just about 10 seconds. Compared to Shap-E, the SOT map of our method only incurs an additional expense of 3.2 A100 seconds (See Tab. 1) which is marginal for 3D generation tasks, but improves substantially in all metrics, especially in FID score.

In addition, we also compared our HOTS3D with a latest score distillation sampling based methods 3DFuse [77] on 100 texts. Results of 3DFuse on FID \downarrow /ViT-B32 \uparrow /L142 \uparrow are 148/82/83 with 2.4k seconds v.s. 43/79/80 of ours with 10 seconds per text, showing better efficiency and semantic quality of our method.

4.2.3 Qualitative Results

The qualitative comparison is presented in Fig. 5, indicating that the baseline methods [2], [8], [18], [33] encounter challenges in generating precise and realistic 3D objects, resulting in semantic inconsistency or incomplete 3D shapes. The results of CLIP-Forge exhibit significant grid artifacts and have low consistency with the text. PureCLIPNeRF can produce 3D content with richer textures and colors, significantly improving text consistency, but has poor control over the geometric shape of the target object. TAPS3D tends to generate simple-styled tables and chairs, while Shap-E lacks control over the geometric shape of objects, both of them need to improve their semantic consistency. SDFusion’s results are more reasonable than the aforementioned baselines, but there is also an obvious issue of text and shape mismatch. In contrast, our method generated more semantically coherent and higher-quality 3D objects by incorporating the SOT map to align text features and shape

features. For instance, for the “*U shaped legs*” in the first row, for the “*2 tables hooked together*” in the third row, and the “*mix rexine material*” in the fifth row, the 3D shapes generated by our model match the text very well. In addition, our results are better in terms of detail and overall quality.

4.2.4 Visual explanation of SOT

To demonstrate the effectiveness of the proposed SOT algorithm in section 3.2, we conducted validation experiments on synthesized spherical data, and the visualization results are shown in Fig. 6. Here, we employed Mollweide projection [78] and vertical projection to visualize the results. The Mollweide projection is an area-preserving [79] projection generally used for maps of the world or celestial sphere. It trades accuracy of angle and shape for accuracy of proportions in area, making it useful for maps depicting global distributions. Specifically, in the first three columns of Fig. 6, we used Mollweide projection, and in the last column, we employed vertical projection to provide different viewing perspectives. In the first row of Fig. 6, the source domain data \mathbf{X} follows four modes *Von Mises-Fisher distribution* (vMF) [80], while the target data \mathbf{Y} follows *uniform distribution on two discontinuous one-eighth spheres*. In the second row, the source \mathbf{X} follows single mode *Von Mises-Fisher distribution* and the target \mathbf{Y} follows six modes *Von Mises-Fisher distribution*.

The vMF distribution is a distribution on S^{d-1} characterized by a concentration parameter $\kappa > 0$ and a location parameter $\mu \in S^{d-1}$ through the density

$$\forall \theta \in S^{d-1}, f_{\text{vMF}}(\theta; \mu, \kappa) = \frac{\kappa^{d/2-1}}{(2\pi)^{d/2} I_{d/2-1}(\kappa)} \exp(\kappa \mu^T \theta), \quad (18)$$

where $I_\nu(\kappa) = \frac{1}{2\pi} \int_0^\pi \exp(\kappa \cos(\theta)) \cos(\nu\theta) d\theta$ is the modified Bessel function of the first kind. It is often referred to as the analogous of the Gaussian distribution on the hypersphere [81].

Specifically, we set the mean direction (μ in Euclidean space) to $(1, 0, 0)$, $(0, 1, 0)$, $(-1, 0, 0)$ and $(0, -1, 0)$ respectively, and then adopt commonly used open source code¹ to generate a mixed vMF distribution with 4 modes. For the target data \mathbf{Y} , we uniformly sampled on two discontinuous one-eighth spheres, whose elevation θ and azimuth φ ranges are $\frac{\pi}{3} \leq \theta \leq \frac{5\pi}{6}$, $0 \leq \varphi \leq \frac{\pi}{2}$ and $\frac{\pi}{3} \leq \theta \leq \frac{5\pi}{6}$, $\frac{\pi}{2} + \frac{\pi}{12} \leq \varphi \leq \pi + \frac{\pi}{12}$, respectively.

For another experiment shown in the second row in Fig. 6, we set the mean direction to $(1, 0, 0)$, $(0, 1, 0)$, $(0, 0, 1)$, $(-1, 0, 0)$, $(0, -1, 0)$, and $(0, 0, -1)$ respectively to generate a mixed vMF distribution with 6 modes, and take it as the target distribution. Then, we set the mean direction as $(1, 0, 0)$ to generate a single mode vMF distribution and take it as the source distribution.

From the results on the right, it can be seen that the distribution of $T(\mathbf{X})$ obtained from our SOT map can align well with the target distribution of \mathbf{Y} . This demonstrates that the proposed SOT map not only effectively maintains clear boundaries between discontinuous regions, but also approximates target distributions with intricate support.

1. <https://github.com/dlwhittenbury/von-Mises-Fisher-Sampling/>

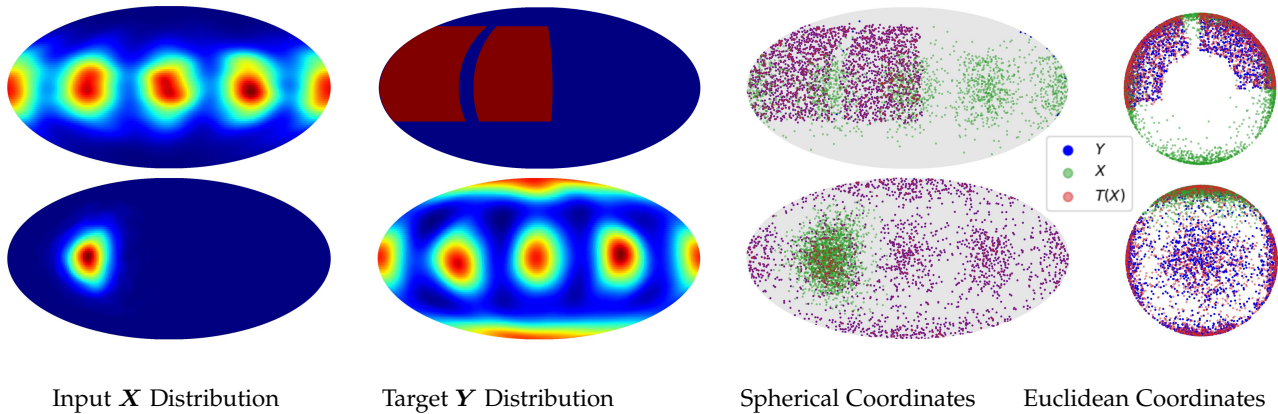


Fig. 6: Visualization of two SOT map results. The first two columns indicate distributions of input and target, respectively (warmer color means higher probability). The last two columns are the visualization of the input point set \mathbf{X} , target point set \mathbf{Y} , and mapped results of SOT $T(\mathbf{X})$ by Mollweide projection and vertical projection, respectively. More overlap between pink SOT mapped results and blue target indicates higher accuracy. Here, the distribution of $T(\mathbf{X})$ is highly consistent with \mathbf{Y} , and $T(\mathbf{X})$ effectively covers \mathbf{Y} well (overlap of pink and blue).

4.2.5 Diversity of generated contents

The proposed HOTS3D has a notable level of creativity. As illustrated in Fig. 7, it can generate varied 3D models even with the same text prompt. In the first row of Fig. 7, the first two generated tables exhibit significant differences in leg design, yet both effectively maintain consistency with the text prompt. As the text on the top right does not specify strict constraints on the shape, our HOTS3D creatively explores the geometric shapes of both the tabletop and table legs. For the chairs in the second row, our model innovatively designs the armrests and backrests while ensuring alignment with the textual description. For the fourth text, the results generated by our model not only meet the descriptions like “wooden material”, “thick rectangular top” and “four small legs”, but also present diverse combinations of tabletops and legs. Moreover, as shown in Fig. 8, our model can generalize to handle text with diverse categories not seen at training such as umbrella, car, and computer.



Fig. 7: Diversity: different 3D shapes generated with the same text prompt input.

We also provide some intriguing results generated by our methods. In Fig. 9, there are examples of some unusually shaped chairs and tables, that are not typically found in the real world but align well with their input text descriptions. This indicates that our method is not only effective in managing the correspondence task between text and shape



Fig. 8: Shapes generated with unseen categories.

during 3D generation but also possesses a notable level of creativity and the ability to generate diverse 3D content.

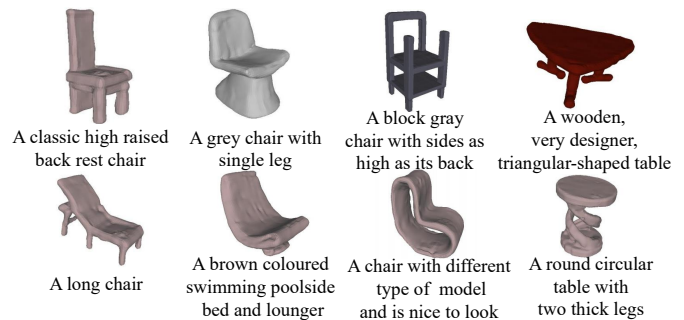


Fig. 9: Visualization of creativity: some interesting but rarely seen 3D objects in the real world.

4.2.6 Ablation Studies

Although many parameters exist (e.g., Generator and NeRF), actually most of them are frozen as Fig. 2 demonstrates. As for the ICNNs [26], a typical structure is adopted. To evaluate the effectiveness of the major component $\mathcal{L}_{fide} = \mathbb{E}_{\mu_S} d(T_f(\mathbf{X}), \mathbf{Y})$ in the optimization objective function (16) of the Kantorovich potential f , we conduct the ablation study in two cases: (A) Without \mathcal{L}_{fide} ; (B) With \mathcal{L}_{fide} . Tab. 2 summarizes the results of each case in terms of CLIP R-Precision and FID score. From the results, it can be seen that \mathcal{L}_{fide} can significantly improve the performance of the generative model, especially in the CLIP R-Precision metric.

Methods	\mathcal{L}_{fide}	CLIP R-Precision	FID
A	×	68.5	50.2
B	✓	80.1	42.6

TABLE 2: Ablation with regular term of objective function

The reason behind this is that \mathcal{L}_{fide} provides one-to-one supervision of text and images. By comparing with our full objective function (bottom row), the necessity of \mathcal{L}_{fide} can be validated.

5 CONCLUSION

In this paper, we propose a novel text-to-3D generation framework in combination with hyper-spherical optimal transport, i.e. **HOTS3D**, which can generate diverse and plausible 3D shapes from text prompts. Our method constructs the SOT map from the text feature hyper-sphere to the image feature hyper-sphere, achieving alignment between text and image features, while also compensating for the missing detailed information in high-level texts to some extent. The experimental results on synthetic data demonstrate the effectiveness of the proposed SOT algorithm. To address the text-to-3D generation, we utilized a pre-trained diffusion-based conditional generator and a controlled NeRF model to transform the aligned feature into 3D content. Our method is shown to generate 3D shapes with superior text semantic consistency compared to previous works, as demonstrated by extensive comparative experiments.

One limitation of our approach is the necessity for the pairing of text and image features to solve the SOT map, which limits the application scenarios of the algorithm. Additionally, optimizing two convex functions simultaneously during training can result in computational waste. In the future, we will study simplifying computational architecture.

REFERENCES

- [1] N. Lei, Z. Li, Z. Xu, Y. Li, and X. Gu, "What's the situation with intelligent mesh generation: A survey and perspectives," *IEEE Transactions on Visualization and Computer Graphics*, 2023.
- [2] A. Sanghi, H. Chu, J. G. Lambourne, Y. Wang, C.-Y. Cheng, M. Fumero, and K. R. Malekshan, "Clip-forge: Towards zero-shot text-to-shape generation," in *Proceedings of the IEEE/CVF Conference on Computer Vision and Pattern Recognition (CVPR)*, June 2022, pp. 18 603–18 613.
- [3] H.-H. Lee and A. X. Chang, "Understanding pure clip guidance for voxel grid nerf models," *arXiv preprint arXiv:2209.15172*, 2022.
- [4] C. Wang, M. Chai, M. He, D. Chen, and J. Liao, "Clip-nerf: Text-and-image driven manipulation of neural radiance fields," in *Proceedings of the IEEE/CVF Conference on Computer Vision and Pattern Recognition (CVPR)*, June 2022, pp. 3835–3844.
- [5] A. Jain, B. Mildenhall, J. T. Barron, P. Abbeel, and B. Poole, "Zero-shot text-guided object generation with dream fields," in *Proceedings of the IEEE/CVF Conference on Computer Vision and Pattern Recognition (CVPR)*, June 2022, pp. 867–876.
- [6] B. Poole, A. Jain, J. T. Barron, and B. Mildenhall, "Dreamfusion: Text-to-3d using 2d diffusion," *arXiv*, 2022.
- [7] C.-H. Lin, J. Gao, L. Tang, T. Takikawa, X. Zeng, X. Huang, K. Kreis, S. Fidler, M.-Y. Liu, and T.-Y. Lin, "Magic3d: High-resolution text-to-3d content creation," in *Proceedings of the IEEE/CVF Conference on Computer Vision and Pattern Recognition*, 2023, pp. 300–309.
- [8] Y.-C. Cheng, H.-Y. Lee, S. Tulyakov, A. G. Schwing, and L.-Y. Gui, "Sdfusion: Multimodal 3d shape completion, reconstruction, and generation," in *Proceedings of the IEEE/CVF Conference on Computer Vision and Pattern Recognition*, 2023, pp. 4456–4465.
- [9] R. Chen, Y. Chen, N. Jiao, and K. Jia, "Fantasia3d: Disentangling geometry and appearance for high-quality text-to-3d content creation," in *Proceedings of the IEEE/CVF International Conference on Computer Vision (ICCV)*, October 2023.
- [10] Z. Wang, C. Lu, Y. Wang, F. Bao, C. Li, H. Su, and J. Zhu, "Prolificdreamer: High-fidelity and diverse text-to-3d generation with variational score distillation," *Advances in Neural Information Processing Systems*, vol. 36, 2024.
- [11] D. Zhenyu Chen, Y. Siddiqui, H.-Y. Lee, S. Tulyakov, and M. Nießner, "Text2tex: Text-driven texture synthesis via diffusion models," *arXiv e-prints*, pp. arXiv–2303, 2023.
- [12] C. Wang, R. Jiang, M. Chai, M. He, D. Chen, and J. Liao, "Nerf-art: Text-driven neural radiance fields stylization," *IEEE Transactions on Visualization and Computer Graphics*, 2023.
- [13] F. Ibarrola, T. Lawton, and K. Grace, "A collaborative, interactive and context-aware drawing agent for co-creative design," *IEEE Transactions on Visualization and Computer Graphics*, 2023.
- [14] A. Radford, J. W. Kim, C. Hallacy, A. Ramesh, G. Goh, S. Agarwal, G. Sastry, A. Askell, P. Mishkin, J. Clark *et al.*, "Learning transferable visual models from natural language supervision," in *International Conference on Machine Learning*. PMLR, 2021, pp. 8748–8763.
- [15] K. Chen, C. B. Choy, M. Savva, A. X. Chang, T. Funkhouser, and S. Savarese, "Text2shape: Generating shapes from natural language by learning joint embeddings," in *Asian conference on computer vision*. Springer, 2018, pp. 100–116.
- [16] P. Mittal, Y.-C. Cheng, M. Singh, and S. Tulsiani, "Autosdf: Shape priors for 3d completion, reconstruction and generation," in *Proceedings of the IEEE/CVF Conference on Computer Vision and Pattern Recognition (CVPR)*, June 2022, pp. 306–315.
- [17] M. Li, Y. Duan, J. Zhou, and J. Lu, "Diffusion-sdf: Text-to-shape via voxelized diffusion," in *Proceedings of the IEEE/CVF Conference on Computer Vision and Pattern Recognition*, 2023, pp. 12 642–12 651.
- [18] H. Jun and A. Nichol, "Shap-e: Generating conditional 3d implicit functions," *arXiv preprint arXiv:2305.02463*, 2023.
- [19] N. M. Khalid, T. Xie, E. Belilovsky, and P. Tiberiu, "Clip-mesh: Generating textured meshes from text using pretrained image-text models," *SIGGRAPH Asia 2022 Conference Papers*, December 2022.
- [20] J. Xu, X. Wang, W. Cheng, Y.-P. Cao, Y. Shan, X. Qie, and S. Gao, "Dream3d: Zero-shot text-to-3d synthesis using 3d shape prior and text-to-image diffusion models," in *Proceedings of the IEEE/CVF Conference on Computer Vision and Pattern Recognition*, 2023, pp. 20 908–20 918.
- [21] V. Seguy, B. B. Damodaran, R. Flamary, N. Courty, A. Rolet, and M. Blondel, "Large-scale optimal transport and mapping estimation," in *ICLR 2018-International Conference on Learning Representations*, 2018, pp. 1–15.
- [22] Y. Chen, M. Telgarsky, C. Zhang, B. Bailey, D. Hsu, and J. Peng, "A gradual, semi-discrete approach to generative network training via explicit wasserstein minimization," *International Conference on Machine Learning*, pp. 1071–1080, 2019.
- [23] D. An, Y. Guo, N. Lei, Z. Luo, S.-T. Yau, and X. Gu, "Ae-ot: A new generative model based on extended semi-discrete optimal transport," *ICLR 2020*, 2019.
- [24] H. Liu, X. Gu, and D. Samaras, "Wasserstein gan with quadratic transport cost," *Proceedings of the IEEE/CVF international conference on computer vision*, pp. 4832–4841, 2019.
- [25] Z. Li, S. Li, Z. Wang, N. Lei, Z. Luo, and X. Gu, "Dpm-ot: A new diffusion probabilistic model based on optimal transport," in *Proceedings of the IEEE International Conference on Computer Vision*, 2023.
- [26] B. Amos, L. Xu, and J. Z. Kolter, "Input convex neural networks," in *International Conference on Machine Learning*. PMLR, 2017, pp. 146–155.
- [27] C. Villani, *Optimal Transport: Old and New*. Springer Science & Business Media, 2008, vol. 338.
- [28] X. Long, Y.-C. Guo, C. Lin, Y. Liu, Z. Dou, L. Liu, Y. Ma, S.-H. Zhang, M. Habermann, C. Theobalt *et al.*, "Wonder3d: Single image to 3d using cross-domain diffusion," *arXiv preprint arXiv:2310.15008*, 2023.
- [29] W. Li, R. Chen, X. Chen, and P. Tan, "Sweetdreamer: Aligning geometric priors in 2d diffusion for consistent text-to-3d," 2023.
- [30] Z. Liu, Y. Li, Y. Lin, X. Yu, S. Peng, Y.-P. Cao, X. Qi, X. Huang, D. Liang, and W. Ouyang, "Unidream: Unifying diffusion priors for relightable text-to-3d generation," *arXiv preprint arXiv:2312.08754*, 2023.

- [31] Y. Yamada, K. Chandu, Y. Lin, J. Hessel, I. Yildirim, and Y. Choi, "L3go: Language agents with chain-of-3d-thoughts for generating unconventional objects," *arXiv preprint arXiv:2402.09052*, 2024.
- [32] G. Nam, M. Khlifi, A. Rodriguez, A. Tono, L. Zhou, and P. Guerrero, "3D-LDM: Neural implicit 3D shape generation with latent diffusion models," *arXiv preprint arXiv:2212.00842*, 2022.
- [33] J. Wei, H. Wang, J. Feng, G. Lin, and K.-H. Yap, "Taps3d: Text-guided 3d textured shape generation from pseudo supervision," in *Proceedings of the IEEE/CVF Conference on Computer Vision and Pattern Recognition*, 2023, pp. 16 805–16 815.
- [34] A. Sanghi, R. Fu, V. Liu, K. D. Willis, H. Shayani, A. H. Khasahmadi, S. Sridhar, and D. Ritchie, "Clip-sculptor: Zero-shot generation of high-fidelity and diverse shapes from natural language," in *Proceedings of the IEEE/CVF Conference on Computer Vision and Pattern Recognition*, 2023, pp. 18 339–18 348.
- [35] J. Tang, J. Ren, H. Zhou, Z. Liu, and G. Zeng, "Dreamgaussian: Generative gaussian splatting for efficient 3d content creation," in *The Twelfth International Conference on Learning Representations*, 2023.
- [36] J. Li, H. Tan, K. Zhang, Z. Xu, F. Luan, Y. Xu, Y. Hong, K. Sunkavalli, G. Shakhnarovich, and S. Bi, "Instant3d: Fast text-to-3d with sparse-view generation and large reconstruction model," in *The Twelfth International Conference on Learning Representations*, 2023.
- [37] Z. Chen, F. Wang, and H. Liu, "Text-to-3d using gaussian splatting," *arXiv preprint arXiv:2309.16585*, 2023.
- [38] Z. Liu, Y. Wang, X. Qi, and C.-W. Fu, "Towards implicit text-guided 3d shape generation," in *Proceedings of the IEEE/CVF Conference on Computer Vision and Pattern Recognition*, 2022, pp. 17 896–17 906.
- [39] R. Fu, X. Zhan, Y. Chen, D. Ritchie, and S. Sridhar, "Shapecrafter: A recursive text-conditioned 3d shape generation model," *Advances in Neural Information Processing Systems*, vol. 35, pp. 8882–8895, 2022.
- [40] X. Tian, Y.-L. Yang, and Q. Wu, "Shapescaffolder: Structure-aware 3d shape generation from text," in *Proceedings of the IEEE/CVF International Conference on Computer Vision*, 2023, pp. 2715–2724.
- [41] Z. Liu, P. Dai, R. Li, X. Qi, and C.-W. Fu, "Iss: Image as stepping stone for text-guided 3d shape generation," *arXiv preprint arXiv:2209.04145*, 2022.
- [42] —, "Dreamstone: Image as a stepping stone for text-guided 3d shape generation," *IEEE Transactions on Pattern Analysis and Machine Intelligence*, 2023.
- [43] L. Qiu, G. Chen, X. Gu, Q. Zuo, M. Xu, Y. Wu, W. Yuan, Z. Dong, L. Bo, and X. Han, "Richdreamer: A generalizable normal-depth diffusion model for detail richness in text-to-3d," *arXiv preprint arXiv:2311.16918*, 2023.
- [44] J. Li, R. Selvaraju, A. Gotmare, S. Joty, C. Xiong, and S. C. H. Hoi, "Align before fuse: Vision and language representation learning with momentum distillation," *Advances in neural information processing systems*, vol. 34, pp. 9694–9705, 2021.
- [45] Q. Cheng, Y. Zhou, P. Fu, Y. Xu, and L. Zhang, "A deep semantic alignment network for the cross-modal image-text retrieval in remote sensing," *IEEE Journal of Selected Topics in Applied Earth Observations and Remote Sensing*, vol. 14, pp. 4284–4297, 2021.
- [46] C. Guo, X. Zuo, S. Wang, and L. Cheng, "Tm2t: Stochastic and tokenized modeling for the reciprocal generation of 3d human motions and texts," in *European Conference on Computer Vision*. Springer, 2022, pp. 580–597.
- [47] Z. Zhu, X. Ma, Y. Chen, Z. Deng, S. Huang, and Q. Li, "3d-vista: Pre-trained transformer for 3d vision and text alignment," in *Proceedings of the IEEE/CVF International Conference on Computer Vision*, 2023, pp. 2911–2921.
- [48] J. Nie, T. Zhang, T. Li, S. Yu, X. Li, and Z. Wei, "Image-based 3d model retrieval via disentangled feature learning and enhanced semantic alignment," *Information Processing & Management*, vol. 60, no. 2, p. 103159, 2023.
- [49] Y. Cao, Z. Yihan, H. Xu, and D. Xu, "Coda: Collaborative novel box discovery and cross-modal alignment for open-vocabulary 3d object detection," *Advances in Neural Information Processing Systems*, vol. 36, 2024.
- [50] Z. Zhao, W. Liu, X. Chen, X. Zeng, R. Wang, P. Cheng, B. Fu, T. Chen, G. Yu, and S. Gao, "Michelangelo: Conditional 3d shape generation based on shape-image-text aligned latent representation," *Advances in Neural Information Processing Systems*, vol. 36, 2024.
- [51] A. Dornitz and A. Tannenbaum, "Texture mapping via optimal mass transport," *IEEE transactions on visualization and computer graphics*, vol. 16, no. 3, pp. 419–433, 2009.
- [52] Z. Li, W. Wang, N. Lei, and R. Wang, "Weakly supervised point cloud upsampling via optimal transport," in *ICASSP 2022-2022 IEEE International Conference on Acoustics, Speech and Signal Processing (ICASSP)*. IEEE, 2022, pp. 2564–2568.
- [53] Z. Li, N. Lei, J. Shi, and H. Xue, "Real-world super-resolution under the guidance of optimal transport," *Machine Vision and Applications*, vol. 33, no. 3, p. 48, 2022.
- [54] Z. Li, S. Li, L. Jin, N. Lei, and Z. Luo, "Ot-net: A reusable neural optimal transport solver," *Machine Learning*, pp. 1–26, 2024.
- [55] X. Gu, Y. Yang, W. Zeng, J. Sun, and Z. Xu, "Keypoint-guided optimal transport with applications in heterogeneous domain adaptation," *Advances in Neural Information Processing Systems*, vol. 35, pp. 14 972–14 985, 2022.
- [56] J. Fan, S. Liu, S. Ma, Y. Chen, and H. Zhou, "Scalable computation of monge maps with general costs," *arXiv preprint arXiv:2106.03812*, p. 4, 2021.
- [57] M. Gazdieva, L. Rout, A. Korotin, A. Filippov, and E. Burnaev, "Unpaired image super-resolution with optimal transport maps," *arXiv preprint arXiv:2202.01116*, 2022.
- [58] J. Xu and G. Durrett, "Spherical latent spaces for stable variational autoencoders," in *Proceedings of the 2018 Conference on Empirical Methods in Natural Language Processing*, 2018, pp. 4503–4513.
- [59] T. R. Davidson, L. Falorsi, N. De Cao, T. Kipf, and J. M. Tomczak, "Hyperspherical variational auto-encoders," in *34th Conference on Uncertainty in Artificial Intelligence 2018, UAI 2018*. Association For Uncertainty in Artificial Intelligence (AUAI), 2018, pp. 856–865.
- [60] X. Gu, J. Sun, and Z. Xu, "Spherical space domain adaptation with robust pseudo-label loss," in *Proceedings of the IEEE/CVF Conference on Computer Vision and Pattern Recognition (CVPR)*, June 2020.
- [61] C. Bonet, P. Berg, N. Courty, F. Septier, L. Drumetz, and M. T. Pham, "Spherical sliced-wasserstein," in *The Eleventh International Conference on Learning Representations*, 2022.
- [62] L. Cui, X. Qi, C. Wen, N. Lei, X. Li, M. Zhang, and X. Gu, "Spherical optimal transportation," *Computer-Aided Design*, vol. 115, pp. 181–193, 2019.
- [63] B. F. Hamfeldt and A. G. Turnquist, "A convergent finite difference method for optimal transport on the sphere," *Journal of Computational Physics*, vol. 445, p. 110621, 2021.
- [64] —, "A convergence framework for optimal transport on the sphere," *Numerische Mathematik*, vol. 151, no. 3, pp. 627–657, 2022.
- [65] S. Cohen, B. Amos, and Y. Lipman, "Riemannian convex potential maps," in *International Conference on Machine Learning*. PMLR, 2021, pp. 2028–2038.
- [66] D. J. Rezende and S. Racanière, "Implicit riemannian concave potential maps," *arXiv preprint arXiv:2110.01288*, 2021.
- [67] C. Villani et al., *Optimal transport: old and new*. Springer, 2009, vol. 338.
- [68] N. Lei, K. Su, L. Cui, S.-T. Yau, and X. D. Gu, "A geometric view of optimal transportation and generative model," *Computer Aided Geometric Design*, vol. 68, pp. 1–21, 2019.
- [69] N. Lei, D. An, Y. Guo, K. Su, S. Liu, Z. Luo, S.-T. Yau, and X. Gu, "A geometric understanding of deep learning," *Engineering*, vol. 6, no. 3, pp. 361–374, 2020.
- [70] A. Makkuva, A. Taghvaei, S. Oh, and J. Lee, "Optimal transport mapping via input convex neural networks," in *International Conference on Machine Learning*. PMLR, 2020, pp. 6672–6681.
- [71] T. Shen, J. Gao, K. Yin, M.-Y. Liu, and S. Fidler, "Deep marching tetrahedra: a hybrid representation for high-resolution 3d shape synthesis," *Advances in Neural Information Processing Systems*, vol. 34, pp. 6087–6101, 2021.
- [72] B. O. Community, *Blender - a 3D modelling and rendering package*. Blender Foundation, Stichting Blender Foundation, Amsterdam, 2018. [Online]. Available: <http://www.blender.org>
- [73] M. Heusel, H. Ramsauer, T. Unterthiner, B. Nessler, and S. Hochreiter, "Gans trained by a two time-scale update rule converge to a local nash equilibrium," *Advances in neural information processing systems*, vol. 30, 2017.
- [74] D.-Y. Chen, X.-P. Tian, Y.-T. Shen, and M. Ouhyoung, "On visual similarity based 3d model retrieval," in *Computer graphics forum*, vol. 22, no. 3. Wiley Online Library, 2003, pp. 223–232.
- [75] D. H. Park, S. Azadi, X. Liu, T. Darrell, and A. Rohrbach, "Benchmark for compositional text-to-image synthesis," in *Thirty-fifth Conference on Neural Information Processing Systems Datasets and Benchmarks Track (Round 1)*, 2021.

- [76] D. P. Kingma and J. Ba, "Adam: A method for stochastic optimization," *arXiv preprint arXiv:1412.6980*, 2014.
- [77] J. Seo, W. Jang, M.-S. Kwak, H. Kim, J. Ko, J. Kim, J.-H. Kim, J. Lee, and S. Kim, "Let 2d diffusion model know 3d-consistency for robust text-to-3d generation," in *The Twelfth International Conference on Learning Representations*, 2024.
- [78] M. Lapaine, "Mollweide map projection," *KoG*, vol. 15, no. 15., pp. 7–16, 2011.
- [79] X. Zhao, Z. Su, X. D. Gu, A. Kaufman, J. Sun, J. Gao, and F. Luo, "Area-preservation mapping using optimal mass transport," *IEEE transactions on visualization and computer graphics*, vol. 19, no. 12, pp. 2838–2847, 2013.
- [80] K. V. Mardia, "Statistics of directional data," *Journal of the Royal Statistical Society Series B: Statistical Methodology*, vol. 37, no. 3, pp. 349–371, 1975.
- [81] N. Leonenko, V. Makogin, and M. S. Cadirci, "The entropy based goodness of fit tests for generalized von mises-fisher distributions and beyond," *Electronic Journal of Statistics*, vol. 15, no. 2, pp. 6344–6381, 2021.



Zezeng Li received a B.S. degree from Beijing University of Technology (BJUT) in 2015 and a Ph.D. degree from Dalian University of Technology (DUT) in 2024. His research interests include image processing, point cloud processing, and generative model.



Weimin Wang received a B.S. degree from Shanghai Jiao Tong University in 2009 and a Ph.D. degree from Nagoya University in 2017. He is currently an Associate Professor at Dalian University of Technology. Before joining DUT, he was a researcher at Artificial Intelligence Research Center of AIST from 2018 to 2021. He researches machine perception, scene understanding and interaction from different scales of the 3D physical world, aiming to enable machines to see the world in super vision.



Wenhai Li received a B.S. degree from Nanchang HangKong University in 2022. He's a third-year master's student at Dalian University of Technology. His research interests include computer vision, mesh generation.



Na Lei received her B.S. degree in 1998 and a Ph.D. degree in 2002 from Jilin University. Currently, she is a professor at Dalian University of Technology. Her research interest is the application of modern differential geometry and algebraic geometry to solve problems in engineering and medical fields. She mainly focuses on computational conformal geometry, computer mathematics, and its applications in computer vision and geometric modeling.



Xianfeng Gu received a B.S. degree from Tsinghua University and a Ph.D. degree from Harvard University. He is now a tenured professor in the Department of Computer Science and Applied Mathematics at the State University of New York at Stony Brook. He has won several awards, such as the NSF Career Award of the USA, the Chinese Overseas Outstanding Youth Award, the Chinese Fields Medal, and the Chenxing Golden Prize in Applied Mathematics. Professor Gu's team combines differential geometry, algebraic topology, Riemann surface theory, partial differential equations, and computer science to create a cross-disciplinary "computational conformal geometry", which is widely utilized in computer graphics, computer vision, 3D geometric modeling and visualization, wireless sensor networks, medical images, and other fields.